Journal of Materials Chemistry A

ROYAL SOCIETY OF CHEMISTRY

PAPER

View Article Online
View Journal | View Issue

Cite this: J. Mater. Chem. A, 2023, 11, 14294

Elucidating the electrochemical reaction mechanism of lithium-rich antiperovskite cathodes for lithium-ion batteries as exemplified by $(Li_2Fe)SeO$†

Lennart Singer, ‡[a] M. A. A. Mohamed, ‡[bd] Henrik Hahn,[a] Ignacio G. Gonzalez-Martinez,[b] Martin Hantusch,[b] Karolina Wenelska,[c] Ewa Mijowska,[c] Bernd Büchner,[b] Silke Hampel,[b] Nico Gräßler *[b] and Rüdiger Klingeler*[a]

Received 31st January 2023
Accepted 8th May 2023

DOI: 10.1039/d3ta00552f

rsc.li/materials-a

We report in the context of lithium-rich antiperovskite cathode materials outstanding electrochemical properties of $(Li_2Fe)SeO$, which for the first time was synthesized *via* direct ball-milling. The unique structured material displays an electrochemical cycling performance of 250 mA h g^{-1} at 0.1C when used as a cathode in lithium-ion batteries. Comprehensive electrochemical analysis combined with detailed transmission electron microscopy studies reveal that, above 2.5 V, the multi electron storage mechanism involves conversion of $(Li_2Fe)SeO$ to $Fe_{1-x}Se_x$. Our results furthermore demonstrate the general relevance of our findings to the whole class of antiperovskite cathode materials and present a route to strongly enhance their cell performance by avoiding the degradation path deciphered by our studies.

1 Introduction

The recent discovery of lithium-rich antiperovskites with the general formula $(Li_2TM)ChO$ (TM = Fe, Mn, Co; Ch = S, Se) has extended the field of cathode materials for lithium-ion batteries (LIB). The new class of lithium-rich antiperovskites exhibits promising properties like low cost, non-toxic raw materials used, high lithium-diffusion and the possibility of multi-electron storage per formula unit which renders them promising alternative cathode materials for LIB.[1–4] Among them, based on its superior multi-electron storage and cycling stability, selenium-containing lithium-rich antiperovskites such as $(Li_2Fe)SeO$ are regarded as particularly compelling, competitive cathode candidates. The full potential of antiperovskite-based cathodes could however, up to now, not completely be unleashed.[2,5,6] Two major obstacles are restraining the antiperovskite cathodes. First, the high-temperature solid-state synthesis method previously applied yields rather large particles, which in turn limits the high-current capability, and the synthesis technique is difficult to scale up.[7] Second, while high-voltage anionic electrochemical activity limits the accessible capacity, the associated processes are yet unclear which hinders the development of appropriate strategies to overcome this issue. Our approach to surpass these barriers exploits a novel mechanochemical synthesis method for the lithium-rich antiperovskite $(Li_2Fe)SeO$ which is based on direct ball milling. This method benefits from a controllable, low-temperature, solvent-free process and can be easily scaled-up to the industrial level.[8] Mechanochemical synthesis furthermore allows to vary the synthesis parameters in a wide regime and thereby to tune relevant material properties such as the particle size.[9] This is particularly relevant as the particle size is directly linked to the required ion transport lengths so that tuning the size in turn yields significant changes of the electrochemical properties.[10–12] Importantly, a more detailed look at the occurring high-voltage processes is provided by our purposefully fabricated, unique $(Li_2Fe)SeO$ samples, elucidating the mechanism of multi-electron storage of the lithium-rich antiperovskites. In the previous literature, lithium storage was discussed as a multi-electron storage process involving cationic and anionic contributions.[2,6,13] In particular, $(Li_2Fe)SO$, $(Li_2Fe)SeO$, and the mixed systems $(Li_2Fe)S_{1-x}Se_xO$ have been studied.[2,3,13] By means of *in situ* XAS, *in situ* XRD and Mössbauer spectroscopy, the first two oxidation peaks in the cyclovoltammograms were attributed to the oxidation of Fe^{2+} to Fe^{3+}.[2] In contrast, the exact anionic process associated with sulfur/selenium has not been fully elucidated despite many investigations. Mikhailova *et al.*[2] have proposed that in the region of high voltages (~2.9 V) an anionic

[a]*Kirchhoff Institute for Physics, Heidelberg University, Im Neuenheimer Feld 227, 69120 Heidelberg, Germany. E-mail: klingeler@kip.uni.heidelberg.de*

[b]*Leibniz Institute for Solid State and Materials Research Dresden e.V., 01069 Dresden, Germany. E-mail: n.graessler@ifw-dresden.de*

[c]*Nanomaterials Physicochemistry Department, Faculty of Chemical Technology and Engineering, West Pomeranian University of Technology, 71-065 Szczecin, Poland*

[d]*Department of Physics, Faculty of Science, Sohag University, 82524 Sohag, Egypt*

† Electronic supplementary information (ESI) available. See DOI: https://doi.org/10.1039/d3ta00552f

‡ Both authors contributed equally.

sulfur reaction S^{-2} to S^0 takes place. The data however did not allow to unambiguously conclude whether this involves an irreversible phase transformation of the antiperovskite (formation of pure amorphous sulfur), or a reversible reaction of the antiperovskite material itself.[2] Further investigations on this issue are essential as knowledge of the complete underlying reaction mechanism is of utmost importance for possible improvement of the electrochemical performance.

Here, we report on two differently synthesized $(Li_2Fe)SeO$ materials with different physical and electrochemical properties. Our studies on the one hand yield insight into the effect and the great potential of mechanochemical synthesis and, on the other hand, elucidate the electrochemical reaction mechanism of antiperovskites in general. The mechanisms are studied by comprehensive electrochemical analyses with a particular focus on the distinct electrochemical processes and their interrelationships accompanied by in-depth transmission electron microscopy. Comparing studies on $(Li_2Fe)SO$ and $(Li_2Fe)SeO$ show that our findings concerning the high-voltage process can be generalised to the whole class of antiperovskites. The such obtained knowledge on the influence of the high voltage process yields a strategy to strongly improve cycling stability and high current capability as demonstrated by our studies on $(Li_2Fe)SeO$. In particular, the here presented $(Li_2Fe)SeO$ does not only display high specific capacity of 250 mA h g^{-1} at 0.1C but also exhibits outstanding high-current performance of 150 mA h g^{-1} after 100 cycles at 1C. Our results hence show the route to improve lithium-rich antiperovskites cathode materials in general, thereby opening the field for further research and improvements in this whole class of materials.

2 Experimental section

2.1 Synthesis

Quantities of Li_2O, Fe and Se as starting materials (purchased from Alfa Aesar), were loaded into a stainless-steel jar inside an argon-filled glovebox according to the desired stoichiometry. The mixture (in total 2 g) was ball-milled using high-energy SPEX SamplePrep 8000D with hardened stainless-steel balls (2 balls 12 mm diameter and 2 balls 6 mm diameter) for 8 h. The powder-to-ball mass ratio was $\sim$1 : 10. After milling, the jar was opened inside the glovebox and a black powder was taken out for further characterization. For the heat treatment of the sample after ball milling, a certain amount of the sample was filled in a corundum crucible (Aliaxis, Frialit-Degussite, AL23) in the glovebox. The crucible was placed into a silica tube (QSILAG; Quarzschmelze, Ilmenau) and temporarily closed with a rubber stopper. Outside the glovebox, the tube was evacuated to a pressure of less than 10^{-3} mbar, refilled with Ar to adjust the internal pressure to 0.2 bar, and sealed with a gas burner. Finally, the closed ampoule was placed into a furnace and heated up to 600 °C (heating rate: 50 °C h^{-1}) for 3 h. The materials obtained by ball milling will be labeled by the suffix '-BM' (*i.e.*, $(Li_2Fe)SeO$-BM) and the potential post-heat treatment temperature may be added, *i.e.*, $(Li_2Fe)SeO$-BM600 refers to a ball-milled material subsequently heated at 600 °C.

2.2 X-ray diffraction (XRD)

The purity and crystallinity of the prepared $(Li_2Fe)SeO$ samples were studied by XRD (STOE STADI P diffractometer) using Debye–Scherrer mode with Co $K_{\alpha 1}$ radiation source (λ = 1.788965 Å) and a Mythen 1 K detector (Dectris). To prevent any air exposure during XRD measurements, the samples were filled into glass capillaries (diameter: 0.6 mm) inside the Ar-filled glovebox and subsequently melt-sealed outside. The XRD patterns were fitted by Voigt function and the sample broadening β_s was derived by subtracting the instrumental broadening β_i from the total broadening β_t as described elsewhere.[14] The average crystallite size (D_{XRD}) was calculated from Debye–Scherrer equation $D_{XRD} = K\lambda/\beta_s \cos(\theta)$, where K is the shape factor, λ is the wavelength of the XRD source, β_s is the full width at half maximum, and θ is the Bragg position.[15]

2.3 Elemental analysis

To estimate the stoichiometry of the produced compositions in terms of molar ratios of the elements, inductively coupled plasma-optical emission spectroscopy (ICP-OES) (iCAP 6500 Duo View, Fa. Thermo Fisher Scientific GmbH) was used.

2.4 X-ray photoelectron spectroscopy (XPS)

X-ray photoelectron spectroscopy (XPS) was performed with a PHI 5600 spectrometer (Physical Electronics) using monochromatic Al-K_α radiation (250 W) equipped with a hemispherical analyzer with 29.35 eV pass energy for high-resolution spectra. To prevent any air exposure the sample was transferred from the glovebox to the XPS device in a special transfer chamber. The estimated spot size on the sample is about 0.4 mm. To avoid charging effects, an electron gun is used as a neutralizer for each measurement.

2.5 Electron microscopy

Scanning electron microscopy (Nova-NanoSEM 200) coupled with energy dispersive spectroscopy (EDS) was used to evaluate the morphology and composition for the compounds under study. High-resolution transmission Electron Microscopy (HR-TEM) studies were performed using a FEI Titan 80-300, equipped with a C_s corrector and operated at 300 kV. The sample was loaded by direct contact onto Cu 300 mesh TEM grids (Agar) and holey carbon film (Plano). For monitoring the micro-structural changes of $(Li_2Fe)SeO$ during cycling, TEM images were acquired using a FEI Titan 80-300 transmission electron microscope, respectively. The *d*-spacings between the atomic fringes in TEM images were evaluated using Digital Micrograph software from Gatan.[16] For each crystalline domain, the average value for the *d*-spacing was calculated from multiple lines at various locations. As uncertainty, the maximum deviation of the measured *d*-spacings to the mean was used. The cycled electrodes were disassembled in an Ar-filled glovebox, washed with ethylene carbonate, and then dried overnight. To prevent air exposure the sample was transferred from the glovebox to the device in a special air-tight transfer box.

2.6 Magnetic measurements

Magnetic measurements were performed on $(Li_2Fe)SeO$ powder samples using an MPMS3 magnetometer (Quantum Design). Magnetisation was measured by varying the temperature between 2 and 300 K using zero-field-cooled (ZFC) and field-cooled (FC) protocols at 0.1 T. Isothermal magnetisation was studied at 2 K in magnetic fields up to ±7 T.

2.7 Thermodynamic investigations

Differential thermal analysis (DTA) up to 1200 °C was performed by means of a Setaram DTA 92-2400 (alumina container) under helium atmosphere (heating rate: 10 °C min^{-1}).

2.8 Surface area analysis

N_2 adsorption/desorption measurements of the samples were conducted to analyse the surface area using ASAP 2460 at a relative pressure of $P/P_0 = 0.1–1.0$. Prior to the measurements, samples were degassed at 100 °C under vacuum for 12 h. The specific surface area was calculated by the Brunauer–Emmett–Teller (BET) method.

2.9 Electrochemical measurements

Electrochemical measurements were carried out using a VMP3 potentiostat (BioLogic) at 25 °C. Slurry preparation as well as cell assembly have been performed in an argon-filled glovebox with controlled humidity and oxygen concentration due to the moisture sensitivity of $(Li_2Fe)SeO$. Working electrodes were prepared by mixing the active material (70% wt), carbon black (15% wt) and polyvinylidene fluoride (PVDF, 15% wt) in dry isopropanol. Afterwards the resulting mixture was spread onto a ($Ø$ = 10 mm) aluminum mesh (thickness 0.125 mm). The obtained electrodes were thereafter dried overnight in vacuum, pressed and dried again. The active material mass loading ranged between 3 and 4.5 mg cm^{-2}. During cell assembly Glass fiber (Whatman GF/D) as the separator, pure lithium metal foil (Aldrich) as the counter electrode and as electrolyte 1 M $LiPF_6$ in a mixture of ethylene carbonate and dimethyl carbonate (1 : 1 by weight) have been used. Cyclic voltammetry (CV) and galvanostatic cycle measurements with potential limitation (GCPL) were performed in a coin cell housing (see ref. 17). Note, the theoretical capacity of $(Li_2Fe)SeO$ for the remove/introduce of 1 Li^+ is 162.8 mA h g^{-1} and we attribute the rate 1C to the charge/discharge current required to remove/introduce 1 Li^+ from/into the antiperovskite material within one hour.

3 Results and discussion

3.1 Structure, morphology, and composition

Fig. 1 displays the XRD patterns of the mechanochemical synthesized $(Li_2Fe)SeO$-BM and $(Li_2Fe)SeO$-BM600 together with the reference pattern of $(Li_2Fe)SeO$.[1] For both samples, all observed peaks correspond to the cubic antiperovskite structure with $Pm\bar{3}m$ space group. The absence of any additional peak in both patterns excludes, within the detection limit, the presence of crystalline impurities in both $(Li_2Fe)SeO$ samples. The heat

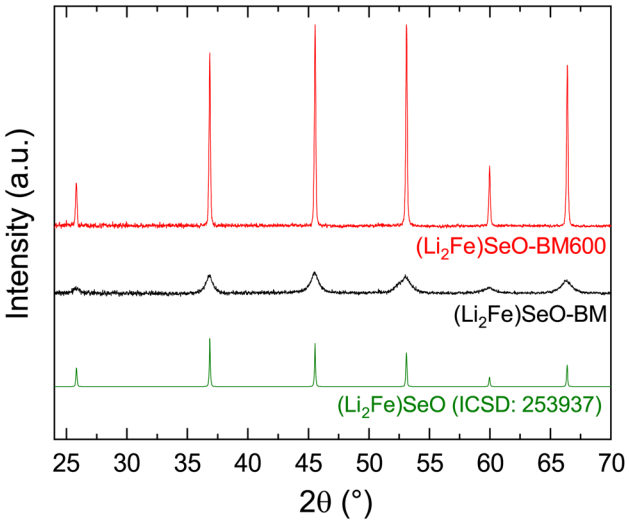

Fig. 1 XRD patterns of $(Li_2Fe)SeO$-BM and $(Li_2Fe)SeO$-BM600 as well as the reference pattern for $(Li_2Fe)SeO$.[1]

treatment leads to an increase in the crystallinity as evident from the higher signal-to-noise ratio for $(Li_2Fe)SeO$-BM600 compared to $(Li_2Fe)SeO$-BM. The lattice parameter in $(Li_2Fe)SeO$-BM amounts to 4.009(2) Å which slightly decreases upon subsequent heat treatment to 4.005(1) Å in $(Li_2Fe)SeO$-BM600. Both values agree well with 4.0025(3) Å reported for $(Li_2Fe)SeO$ prepared by solid-state reaction.[1] The small reduction of the lattice parameter upon heat treatment can likely be attributed to strain relaxation and the vanishing of intrinsic defects such as stacking faults and grain boundaries. By considering the peak broadening and using Debye–Scherrer formula,[15] the crystallite size of 5.2(9) nm for $(Li_2Fe)SeO$-BM and 41(2) nm for $(Li_2Fe)SeO$-BM600 was calculated; the changes upon heat treatment coincides with the expectation on thermal grain-size growth.

To further confirm the formation of $(Li_2Fe)SeO$ and to exclude the presence of other oxidation states, XPS analyses were carried out on $(Li_2Fe)SeO$-BM and $(Li_2Fe)SeO$-BM600. The full XP survey spectra (see Fig. S1 in the ESI†) for both samples confirm the presence of Li, Fe, Se, and O with only a slight contribution of adsorbed atmospheric carbon, which is typical and hard to avoid.[18] For further insight, Fig. 2 shows high-resolution spectra of (a) Li 1s, Se 3d and Fe 3p (b) Fe 2p and (c) Se 3p, Se LMM Auger-peak, and (d) O 1s. The measured spectra in Fig. 2a consist of a combination of the Li 1s, Se 3d, and Fe 3p lines which are all in the energy range between 53 and 56 eV.[19] Due to the strong mixing of these lines, into only one clearly visible peak, it is not possible to accurately quantify the actual surface composition and oxidation state of these elements from the recorded spectra. The fact that the relative sensitivity factor of Fe 3p is 30 times higher than for Li 1s further hinders separation.[20] Fig. 2b presents the Fe 2p spectra and their splitting into two characteristic peaks at 709 eV (Fe $2p_{3/2}$) and 722.2 eV (Fe $2p_{1/2}$) due to spin–orbit coupling. The clearly visible satellite features at higher binding energies compared to the main Fe $2p_{3/2}$ and Fe $2p_{1/2}$ peaks strongly suggest the high-spin state of Fe^{2+} in both materials under

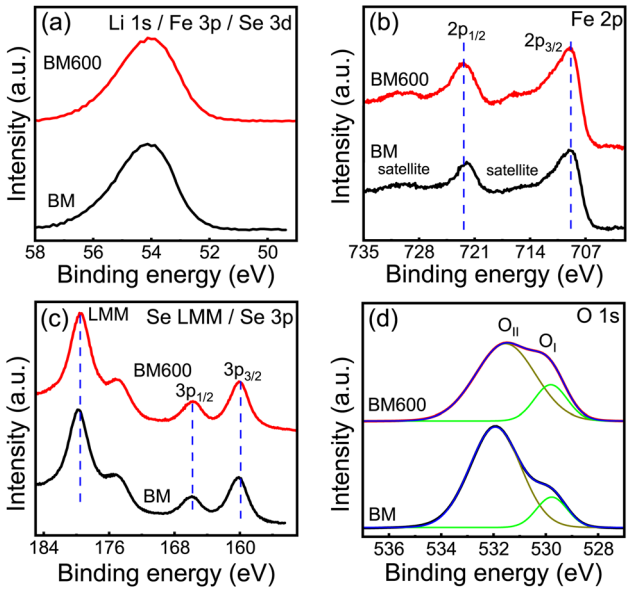

Fig. 2 High-resolution XP spectra of (Li_2Fe)SeO-BM and (Li_2Fe)SeO-BM600 of the (a) Li 1s, Se 3d and Fe 3p, (b) Fe 2p, (c) Se LMM Auger-peak, and (d) O 1s.

study.[21,22] For both materials, the Se 3p and Se LMM peaks shown in Fig. 2c appear in the energy range from 155 eV to 185 eV. The very similar spectra indicate that heat treatment at 600 °C does not significantly affect the selenium oxidation state. The measured binding energies of Se $3p_{3/2}$ (160.2 eV) and Se $3p_{1/2}$ (165.8 eV) are close to reported values for Se^{2-} in CdSe[23] and ZnSe,[24] thereby confirming the oxidation state −2 of selenium in both materials studied at hand. The O 1s spectra of (Li_2Fe)SeO-BM and (Li_2Fe)SeO-BM600 are separated into two peaks, *i.e.*, O_I and O_{II} (see Fig. 2d). The first peak (O_I) appears for both materials at 529.8 eV, while O_{II} locates at 531.9 eV for (Li_2Fe)SeO-BM and at 531.5 eV for (Li_2Fe)SeO-BM600. We attribute O_I to the oxygen lattice, while O_{II} most likely corresponds to chemisorbed oxygen species.[25] The higher relative expression of O_{II} for (Li_2Fe)SeO-BM may indicate a higher amount of absorbed oxygen species due to the smaller particle size and higher specific surface of the material. The hypothesis of a higher specific surface area of (Li_2Fe)SeO-BM compared to -BM600 was confirmed by N_2 adsorption measurements (see Fig. S2†), which show that while both materials exhibit a low surface area, (Li_2Fe)SeO-BM, with 1.2(4) $m^2\ g^{-1}$, has more than twice the surface area of -BM600, with 0.5(1) $m^2\ g^{-1}$. The XPS analysis in summary confirms the successful formation of (Li_2Fe)SeO in both materials. In addition, we observe quasi-identical XP spectra which imply no significant differences in the oxidation states of the contained Se, Li, Fe, and O due to heat treatment. In particular, our data exclude the presence of impurities with different oxidation in both samples.

The morphology and micro-structure of (Li_2Fe)SeO-BM and (Li_2Fe)SeO-BM600 are investigated by SEM and TEM images (see Fig. 3). The SEM image of (Li_2Fe)SeO-BM (Fig. 3a) displays irregular, nearly spherical dominantly sub-micrometer-sized primary particles. Compared to (Li_2Fe)SeO prepared by solid-state synthesis,[3] (Li_2Fe)SeO-BM displays a strongly reduced particle size along with a narrower size distribution. In addition, minor particle agglomeration is visible in the SEM images of (Li_2Fe)SeO-BM which we attribute to the cold welding phenomenon during the milling process.[26] Additional heat treatment leads to strong sintering of the primary fine particles into larger agglomerates (see Fig. 3e of (Li_2Fe)SeO-BM600) which we attribute to the Ostwald repining effect.[27] To confirm the uniform distribution of the elements and the nominal composition, EDS measurements were performed as shown in Fig. S3 and S4.† The EDS analyses reveal uniform distribution of the elements and that both (Li_2Fe)SeO-BM and (Li_2Fe)SeO-BM600 consist entirely of Fe, Se, and O with comparable relative atomic percentages coinciding with the expected stoichiometry. Moreover, no indication of impurities or contamination are detected. The stoichiometric composition of the material is further proven by ICP-OES analysis whose results are presented in Table S1 in the ESI.† The good agreement between the measured and nominal values in addition excludes non-stoichiometric extraneous phases.

TEM images in Fig. 3 provide a closer insight into the morphology and lattice spacings of (Li_2Fe)SeO-BM (b–d) and (Li_2Fe)SeO-BM600 (f–h). The selected area electron diffraction (SAED) pattern of (Li_2Fe)SeO-BM (inset of Fig. 3b) shows that the Bragg peaks are arranged in circles of different diameters. We conclude that the SAED spot area covers several crystallites which is in agreement with the crystallite size of $d_{XRD} \simeq 5$ nm obtained from the Scherrer analysis as well as from crystalline regions in Fig. 3c. The TEM images of (Li_2Fe)SeO-BM furthermore reveal not only multiple crystallites inside a given micro-scaled particle, they also show the existence of two kinds of crystalline regions. The dominant one (Fig. 3c) consists entirely of crystalline domains related to the (Li_2Fe)SeO phase, as evidenced by the appearance of average interplanar spacing of 0.21(1) nm and 0.29(1) nm between the atomic fringes corresponding to (200) and (110) planes of (Li_2Fe)SeO. The data also indicate a second kind of crystalline regions in (Li_2Fe)SeO-BM (see Fig. 3d) that clearly differ from the *d*-spacing values of the (Li_2Fe)SeO phase (Fig. 3d). Specifically, the observed *d*-spacings between 0.54 to 0.56, and 0.31(1) nm can not be associated with the (Li_2Fe)SeO phase so that we conclude the presence of an impurity phase. As the associated layer distances of 0.55(2) and 0.31(1) nm deduced from Fig. 3d match well with the (001) and (101) spacings in tetragonal FeSe,[28] we infer the presence of a FeSe impurity phase in (Li_2Fe)SeO-BM. Note, that crystalline regions with spacings of 0.29(1) and 0.19(1) nm could either correspond within the uncertainty to the (110) and (200) planes in (Li_2Fe)SeO or to the (002) and (112)/(200) planes of FeSe. In addition, the presence of non-stoichiometric FeSe can based on our analysis not be excluded since some regions display a slight deviation of the lattice *d*-spacing of 0.55 nm corresponding to stoichiometric FeSe. As a result of heat treatment after milling ((Li_2Fe)SeO-BM600 sample), the crystallinity improves as indicated by the observation of aligned dots in SAED (see inset in Fig. 3f) and an increase in the size of the crystalline domain corresponding to (110) plane of (Li_2Fe)SeO (Fig. 3g). In addition to crystalline domains corresponding to

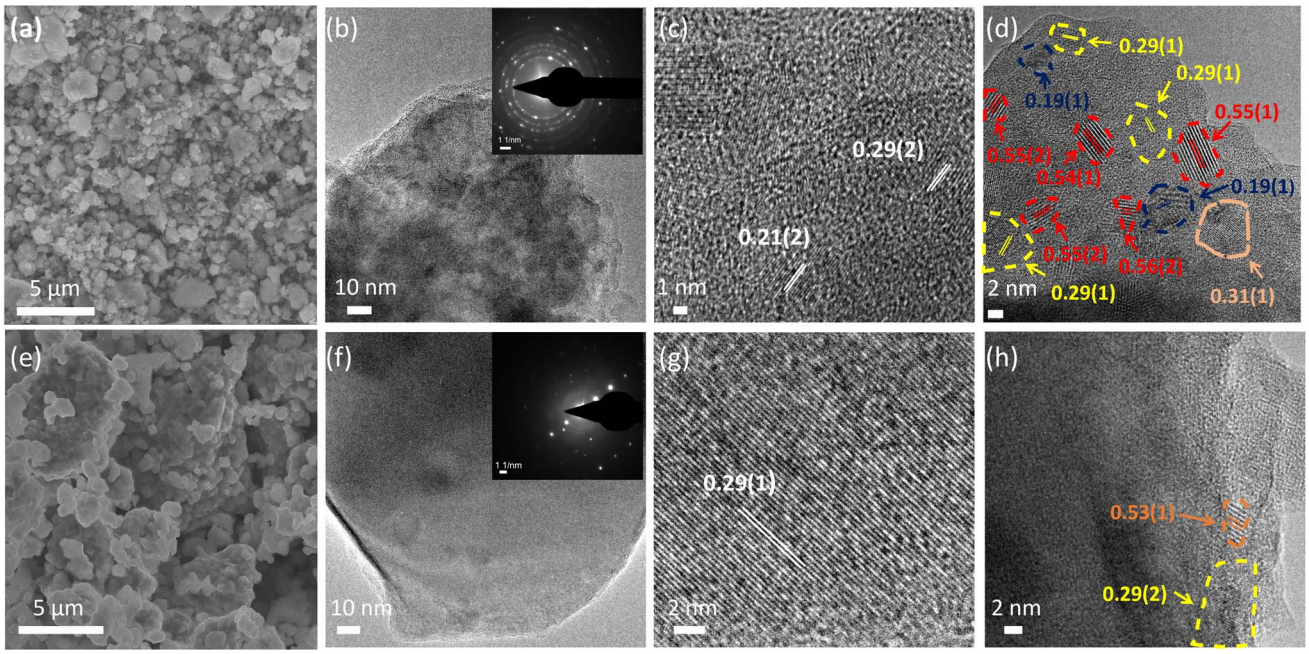

Fig. 3 SEM and HR-TEM images of $(Li_2Fe)SeO$-BM (a–d) and $(Li_2Fe)SeO$-BM600 (e–h). The inset in (b) and (f) displays the obtained SAED pattern. The depicted *d*-spacings are given in the unit nanometer. Differently colored dashed lines in (d) and (h) mark regions with different lattice spacing.

$(Li_2Fe)SeO$ with a *d*-spacing of 0.29(2) nm, $(Li_2Fe)SeO$-BM600 displays only rarely, small crystalline domains with 0.53(1) nm interplanar spacing (Fig. 3h). Regions with a *d*-spacing of 0.53(1) nm may indicate the presence of non-stoichiometric FeSe. The observation that the number as well as the *d*-spacing of crystallite domains corresponding to $Fe_{1-x}Se_x$ decrease in $(Li_2Fe)SeO$-BM600, further supports its assignment to FeSe in $(Li_2Fe)SeO$-BM as tetragonal FeSe is reported to be thermally unstable at high temperatures.[29]

Owing to its characteristic magnetic properties,[30] the presence of small amounts of $Fe_{1-x}Se_x$ is unambiguously confirmed by magnetic studies (see Fig. S5 in the ESI†). Specifically, from the magnetization data we infer the presence of β-$Fe_{1-x}Se$ with $x \approx 0.26$ and of $Fe_{1-x}Se$ with $x \approx 0.21$–0.29.[30–32] Since magnetic order is supposed to appear in crystalline structures, these results indicate crystalline magnetic impurity phases in the low single-digit % regime. In addition, there may be amorphous regions of the same phases.

DTA measurements in the temperature range between room temperature (RT) and 1200 °C show the thermal behavior and stability of ball-milled $(Li_2Fe)SeO$-BM (see Fig. S6a in the ESI†). The DTA results indicate a single endothermic (at 1039(2) °C) and exothermic (at 1018(2) °C) peak corresponding to the melting and re-solidification process of $(Li_2Fe)SeO$, respectively. The absence of any additional process, even though some $Fe_{1-x}Se_x$ is expected from the TEM and magnetisation analysis, may refer to impurity content below the resolution limit of the DTA, its mainly amorphous nature, or both. Similar thermal behavior in the first and the second thermal cycles proves thermal reversibility of the material. In addition, XRD after heating the sample above its melting point and cooling it to room temperature (see Fig. S6b†) confirms congruent melting of $(Li_2Fe)SeO$-BM without any phase transition/decomposition. The observed thermal properties of $(Li_2Fe)SeO$-BM are therefore in good agreement with the reported properties of $(Li_2Fe)SeO$ prepared by the solid-state reaction method.[3] We particularly note that our data imply that $(Li_2Fe)SeO$ antiperovskites possess superior thermal stability as compared to other commercial cathode materials[33] which may be advantageous for Li-ion battery performance at high operating temperatures.

3.2 Electrochemical studies

The mechanochemically synthesized $(Li_2Fe)SeO$-BM as well as the temperature-treated $(Li_2Fe)SeO$-BM600 are studied as cathode material in LIB. The corresponding cyclic voltammograms in the potential range 1 to 3 V *vs.* Li/Li^+ shown in Fig. 4 demonstrate that the two $(Li_2Fe)SeO$ materials exhibit a comparable multistage lithium extraction and insertion mechanism which is also similar to the previous report on $(Li_2Fe)SeO$ produced by the solid state reaction (SSR) method.[3] The open circuit voltage (OCV) of $(Li_2Fe)SeO$-BM (2.1 V) and -BM600 (2.2 V) is in the middle of the electrochemical reactions. Note, a full cyclic voltammetry cycle starts and ends at OCV. For both materials at hand, the two initial oxidation peaks O_1 and O_2 appear at about ~2.3 V and 2.5 V and signal the two-stage cationic Fe^{2+} to Fe^{3+} oxidation process.[2,13] We note the lower voltage of these features compared to $(Li_2Fe)SeO$-SSR.[3] This shift towards lower voltages can be attributed to lower polarization due to the smaller particle sizes and corresponding smaller

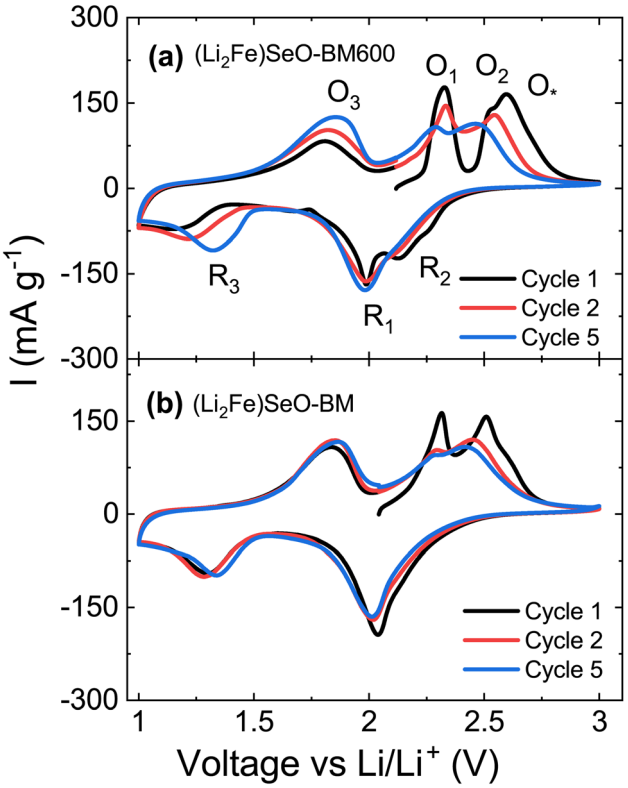

Fig. 4 Cyclic voltammograms of cycle 1, 2 and 5 of (a) $(Li_2Fe)SeO$-BM600 and (b) $(Li_2Fe)SeO$-BM measured at a scan rate of 0.1 mV s^{-1}. The labels R/O mark distinct reduction and oxidation features.

diffusion path length for Li^+.[34–36] An anionic reaction of the contained chalcogen is proposed to take place in the high-voltage region O_2, O_*.[2,13] During the first intercalation (discharge), both samples display distinct reduction peaks (R_1, R_2, R_3) in the CV. Note, the lower distinctness and the higher broadness of the peaks in the cyclic voltammogram of $(Li_2Fe)SeO$-BM can, in accordance with the XRD data, be attributed to the lower crystallinity. By comparing the first cycle with the following ones, it becomes evident that the first cycle is fundamentally different regarding the number, positions and curvature of the peaks, which seems to be a general phenomenon of $(Li_2Fe)SeO$ and other similar antiperovskite compounds. This is particularly visible by the appearance of a fourth pronounced peak O_3 at about ~1.8 V in the second delithiation cycle. This fourth peak is more pronounced in $(Li_2Fe)SeO$-BM600 than in $(Li_2Fe)SeO$-BM and increases in the subsequent cycles. The other peaks (O_1, O_2, O_*) strongly decrease in height upon cycling with a concomitantly increasing overlap. In fact, from the CVs it cannot be unambiguously seen whether O_* is still present after cycle 1 since it becomes indiscernible but might be hidden by O_2. In the intercalation cycles, the change of the subsequent cyclic voltammetry curves is less dominant and mainly visible at the peak R_3. Notably, the peaks R_3/O_3 not only shift but also clearly increase for BM600 whereas for $(Li_2Fe)SeO$-BM the peak height does not change significantly. Overall, upon cycling the CV curves of both materials become more and more similar. This may indicate strong irreversible structural changes of $(Li_2Fe)SeO$ in the initial cycle exceeding the initial effect of a post-synthesis heat treatment.

To investigate the electrochemical processes and their interrelationships, as well as the differences between both materials in more detail, CV measurements in three limited potential ranges (row a, b, and c of Fig. 5) were carried out for both $(Li_2Fe)SeO$ materials. As will be discussed in detail below, these measurements demonstrate the effect and stability of the distinct processes in each regime and allow us to identify the interdependencies between them. Firstly, the CVs with initial lithiation (discharge) to 1 V and restriction of the maximum voltage to OCV (Fig. 5, row a) show the electrochemical behavior upon initial intercalation of the cathode material, thereby allowing to investigate possible lithium vacancies or reactive anodic impurity phases. In phase-pure cathode material without defects and void space, it is not possible to directly incorporate further lithium into the material, which holds especially for the here presented $(Li_2Fe)SeO$ as their stoichiometric and structural composition is confirmed by XRD, XPS, EDS and ICP-EOS. The results for $(Li_2Fe)SeO$-BM however display not only electrochemical activity but also a clearly visible reduction peak R_3 at around 1.4 V and an oxidation peak O_3 at around 1.8 V. The observation of such a redox pair in the CV imply the presence of an electrochemical active foreign phase. Moreover, the process appears to be very stable, which is represented by quasi-perfect overlapping CV curves of $(Li_2Fe)SeO$-BM. For BM600 on the other hand this process is only negligibly pronounced. As the only difference between BM and BM600 is the post-temperature treatment to 600 °C, this implies that the electrochemical active foreign phase is not stable up to this temperature. Both this observation and the peak positions which match literature values for $Fe_{1-x}Se_x$ (ref. 37 and 38) confirm the presence of an electrochemically active $Fe_{1-x}Se_x$ phase as suggested by the TEM and magnetisation studies discussed above. Extending the upper voltage limit to ≈2.4 V (see row b of Fig. 5) includes the peak O_1 and hence allows us to examine the processes associated with the reaction pair O_1/R_1, which is considered to be a part of the reversible redox process ($Fe^{2+} \leftrightarrow Fe^{3+}$). As expected for a reversible intercalation process, an almost perfect overlap of the CV curves of the following cycles can be seen, proving the excellent reversibility of this process. Note, there is also no discernible change in the O_3/R_3 peaks in $(Li_2Fe)SeO$-BM. The CVs extending to the full potential range of 1 to 3 V and thereby including the two high voltage processes O_2 and O_* are displayed in row c of Fig. 5. For both samples, the data imply significant changes driven by the high-voltage processes which in particular involve pronounced non-reversible behavior and the appearance of a new redox pair in $(Li_2Fe)SeO$-BM600. Specifically, the pair R_3/O_3 evolves in the low voltage regime and in both materials it increases and shifts upon cycling. Furthermore, especially for $(Li_2Fe)SeO$-BM600, there is a significant decrease and broadening of O_1, O_2 and O_* in the subsequent cycles after passing through O_2/O_*. It is noteworthy that for $(Li_2Fe)SeO$-BM, the previously visible peak pair R_3/O_3 is also clearly enhanced after passing O_2/O_*. Based on

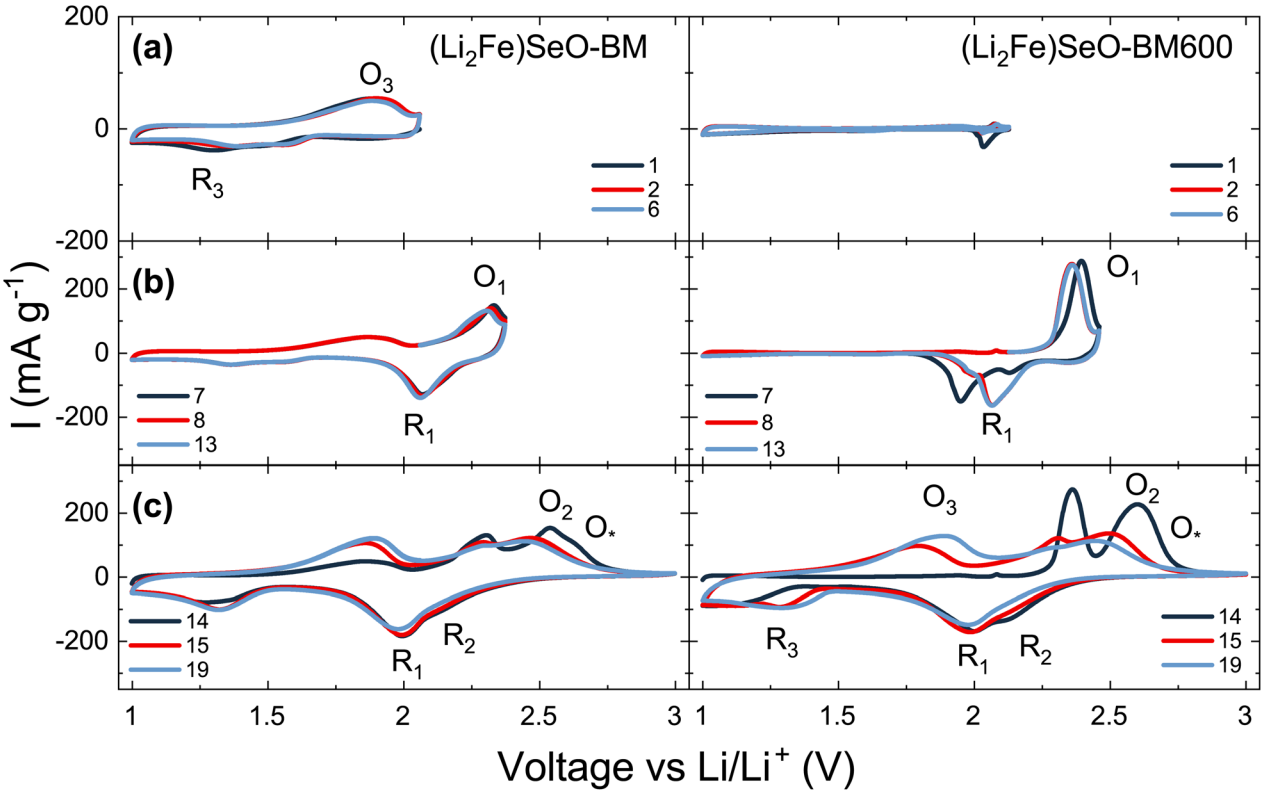

Fig. 5 Cyclic voltammograms of $(Li_2Fe)SeO$-BM and $(Li_2Fe)SeO$-BM600 in the potential range from (a) 1 V to OCV, (b) 1 to 2.38/2.48 V respectively, and (c) 1 to 3 V *vs.* Li/Li^+ measured at a scan rate of 0.1 mV s^{-1}. The labels R/O correspond to the ones in Fig. 4.

our observations, these results demonstrate that passing through the high voltage oxidation processes O_2/O_* triggers an irreversible process that partly converts $(Li_2Fe)SeO$ to a different phase which is electrochemically active as demonstrated by the redox pair R_3/O_3. The peak positions at ~1.4 and 1.8 V, respectively, in both samples strongly suggest that $Fe_{1-x}Se_x$ is formed during the high voltage processes. This is confirmed by the corresponding presence of R_3 in $(Li_2Fe)SeO$-BM signaling the $Fe_{1-x}Se_x$ impurity phase. The additional activity signaled by R_3/O_3 agrees to the expected behaviour of $Fe_{1-x}Se_x$ and further corroborates this conclusion.

To gain detailed information on the charge converted in each of the above-discussed processes and to precisely determine the voltage regime where the irreversible processes O_* start, the maximum potential in GCPL measurements was step-wise increased from OCV to 3 V with a 0.1 V step size (see Fig. S7 in the ESI†). For $(Li_2Fe)SeO$-BM600, the capacity stored by direct discharge from OCV is very small and amounts to only 6 mA h g^{-1}. This agrees to the CVs which show negligible electrochemical activity in this regime. The same measurements on $(Li_2Fe)SeO$-BM however yield the sizable capacity of ~60 mA h g^{-1} for the first three cycles (see Fig. S7a and c in the ESI†). The quasi-linear behaviour of the potential curves hints to the amorphous nature of the electrochemical active $Fe_{1-x}Se_x$. Upon subsequent increase of the potential range, in $(Li_2Fe)SeO$-BM600 a change of the potential lines and the development of a plateau-like feature indicating the low-voltage process R_3/O_3 is seen when the maximum voltage of 2.5 V is exceeded (see Fig. S7d†). For $(Li_2Fe)SeO$-BM the boundary voltage is due to the already initially existing $Fe_{1-x}Se_x$ impurity phase harder to estimate. However, one also observes a change in the potential line profile and an increase of the plateau-like feature (R_3/O_3) in the 2.5 V boundary voltage region. The data, therefore, imply that, at C/10, the limiting voltage to avoid the irreversible transformation of $(Li_2Fe)SeO$ to $Fe_{1-x}Se_x$ is around 2.5 V.

In order to further confirm the formation of $Fe_{1-x}Se_x$ in $(Li_2Fe)SeO$-BM600 during cycling, *ex situ* TEM measurements of $(Li_2Fe)SeO$-BM600 have been performed after charging the material to 3 V using a constant current constant voltage (CCCV) protocol. The TEM results in Fig. 6a–c show that the cycled material again exhibits two kinds of particles. Firstly, there are particles with crystalline structures similar to those observed in the pristine material with lattice spacings corresponding to $(Li_2Fe)SeO$ (Fig. 6a). In addition, the TEM images (Fig. 6b and c) display particles with mixed crystalline/amorphous regions where the crystalline parts exhibit a lattice spacing of 0.55(1) nm corresponding to FeSe.[28] It has to be mentioned that crystalline regions with a large lattice *d*-spacing of 0.53(1) nm are also present in pristine $(Li_2Fe)SeO$-BM600 but very rarely which is in agreement with the electrochemical data. We hence conclude that the highlighted area in (c) correspond to regions where $(Li_2Fe)SeO$ was converted to $Fe_{1-x}Se_x$.

To verify whether the high voltage process O_* and its effects are general, synthesis-independent phenomena in anti-perovskite cathodes, similar measurements were also performed for $(Li_2Fe)SeO$-SSR and $(Li_2Fe)SO$-SSR (see Fig. S8 in the

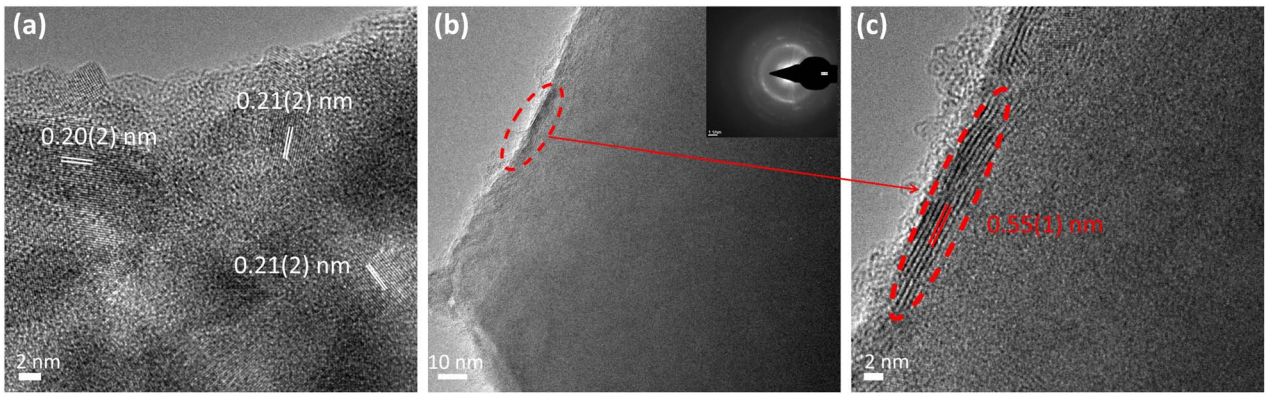

Fig. 6 *Ex situ* TEM images of an $(Li_2Fe)SeO$-BM600 electrode charged to 3 V using a CCCV protocol (see the text).

ESI†). X-ray diffractograms as well as SEM images of the SSR samples can be found in the ESI Fig. S9† and display their purity and particle size. The obtained CVs are very similar to the ball-milled $(Li_2Fe)SeO$ and confirm a highly reversible behaviour when the voltages are limited below the high voltage process O_*. Significant irreversibility appears again only when the high-voltage processes are included. The fact that this observation holds for all presented antiperovskite materials independent on synthesis and composition demonstrates that the process O_* is a general feature of antiperovskite cathodes which strongly hinders reversible cycling.

In summary, we conclude two major results. (1) We find a new process in the high voltage range that leads to the progressive, irreversible phase transformation of $(Li_2Fe)SeO$ to $Fe_{1-x}Se_x$. (2) We discover the severe effect of the process (O_*) on the electrochemical properties of lithium-rich antiperovskites and prove its generic nature.

The current capability of $(Li_2Fe)SeO$-BM and $(Li_2Fe)SeO$-BM600 is displayed in Fig. 7. To determine the influence of O_* on the high-current capability and stability, measurements were conducted both up to 3 V and in a limited potential range (up to 2.5 V) avoiding O_*. At cycle 1, two characteristics stand out. Firstly, in the entire potential range, 1–3 V, both samples convert an enormous initial capacity of around 300 mA h g^{-1} at a current rate of C/10, which is up to now the highest capacity ever reported for any Li-rich antiperovskite and therefore confirms the huge advantage and potential of mechanochemical synthesis. Secondly, in the restricted potential regime a capacity of still 220 mA h g^{-1} is reached for $(Li_2Fe)SeO$-BM and around 150 mA h g^{-1} for $(Li_2Fe)SeO$-BM600. The following nine cycles (see Fig. 7a) illustrate that capacity fading even in the initial cycles is completely different when cycling $(Li_2Fe)SeO$ at up to 3 V and 2.5 V, respectively. For the former range, both $(Li_2Fe)SeO$ samples display a strong decrease in capacity whereas in the restricted potential range $(Li_2Fe)SeO$-BM shows stable capacity and $(Li_2Fe)SeO$-BM600 even an increase to 240 mA h g^{-1} in cycle 10. At higher current rates, these effects become more pronounced: in $(Li_2Fe)SeO$-BM, we observe average capacities of 205, 170, and 136 mA h g^{-1} at C/4, C/2 and 1C in the full potential range and 204, 190, and 163 mA h g^{-1} in the limited one. In $(Li_2Fe)SeO$-BM600, the same measurements yield 150, 108, and 75 mA h g^{-1} (full range) and 196, 145, and 95 mA h g^{-1} (limited range). The major findings are as following: (1) $(Li_2Fe)SeO$-BM exhibits a better overall high current capability than BM600. (2) The limited potential range is beneficial for both samples, leading to a higher converted capacity at higher currents and improved cycling stability. In

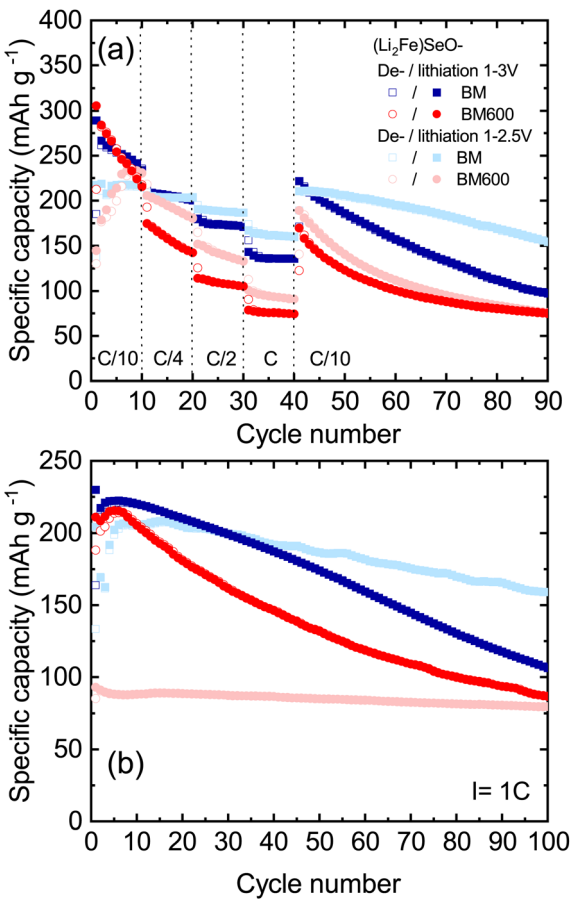

Fig. 7 Rate performance (a) and specific dis-/charge capacities at 1C (b) of $(Li_2Fe)SeO$-BM and -BM600 in the potential window 1–3 V and 1–2.5 V, respectively.

particular, in the limited potential regime the reversibly accessibly capacity in $(Li_2Fe)SeO$ exceeds the one accessible when cycling up to 3 V after a few cycles. We hence also conclude, that the hybrid $(Li_2Fe)SeO/Fe_{1-x}Se_x$ material in $(Li_2Fe)SeO$-BM displays a superior electrochemical performance compared to the pure material present in $(Li_2Fe)SeO$-BM600. However, a part of the converted capacity for $(Li_2Fe)SeO$-BM is associated with the contained $Fe_{1-x}Se_x$-phase. In both cases, application of a limited potential range is beneficial for the electrochemical performance.

The evolution of the potential profiles provides further insight into the differences appearing for the two materials and voltage regimes and in particular where the capacity is actually converted (see Fig. S10 in the ESI†). In agreement with the expected formation of $Fe_{1-x}Se_x$ at high voltages, the associated capacity to the converted capacity of cycle one for the samples $(Li_2Fe)SeO$-BM and BM600 in the full potential range (see Fig. S10a and c†) is already highly increased 112 mA h g^{-1} ($(Li_2Fe)SeO$-BM) and 118 mA h g^{-1} ($(Li_2Fe)SeO$-BM600) compared to the capacity attributed to the $Fe_{1-x}Se_x$-phase which can be obtained by direct discharge (60 mA h g^{-1} and 6 mA h g^{-1} for $(Li_2Fe)SeO$-BM and -BM600). The formed $Fe_{1-x}Se_x$-phase however cannot compensate for the capacity losses of $(Li_2Fe)SeO$, hence resulting in the observed fading. The data also imply that in $(Li_2Fe)SeO$-BM the process O_3/R_3 attributed to $Fe_{1-x}Se_x$ does not increase when cycling in the limited voltage range from 1 to 2.5 V while a clear increase of this process is evident in $(Li_2Fe)SeO$-BM600 already after the fifth cycle. One might speculate that already at 2.5 V a small portion of $Fe_{1-x}Se_x$ is formed in $(Li_2Fe)SeO$-BM600 in contrast to $(Li_2Fe)SeO$-BM which may explain its lower cycling stability in the restricted potential range. This result again indicates the dependence on and importance of the boundary voltage, as slight changes lead to huge effects on the electrochemical performance. Note, that the reversible regime depends on the kinetics present and especially the current rate as all processes shift to higher voltages for higher currents. Comparing the positions of the plateaus in the potential profiles at 1C and C/10 leads to an estimated shift of 0.1 to 0.2 V.

Galvanostatic cycling studies at 1C (Fig. 7b) confirm excellent electrochemical performance of mechanochemically synthesized $(Li_2Fe)SeO$. As already mentioned above, the data in particular imply superior performance of $(Li_2Fe)SeO$-BM when limiting the voltage to a maximum of 2.5 V. Specifically, while the initial capacity amounts to around 200 mA h g^{-1}, cycling at 1C only yields moderate capacity fading resulting in 158 mA h g^{-1}, after 100 cycles. When cycling to 3 V, slightly higher initial capacity of ~220 mA h g^{-1} is achieved with however much stronger fading to 105 mA h g^{-1} in cycle 100. For the same voltage regime, findings for $(Li_2Fe)SeO$-BM600 are similar, *i.e.*, there is a rather larger decrease of capacity from initially 210 mA h g^{-1} to 90 mA h g^{-1} in cycle 100. Whereas, in the limited potential range a quasi-constant capacity of 90 mA h g^{-1} is reached. The latter observation is in full accordance with our conclusion that presence and conversion to $Fe_{1-x}Se_x$ triggers capacity fading in $(Li_2Fe)SeO$ as in $(Li_2Fe)SeO$-BM600 there is no $Fe_{1-x}Se_x$ and due to the slight shift of O_* towards higher voltages (see Fig. S11 in the ESI†) conversion to $Fe_{1-x}Se_x$ starts at 1C well above 2.5 V. Long-term galvanostatic cycling studies of $(Li_2Fe)SeO$-BM and $(Li_2Fe)SeO$-BM600 in the restricted potential range to 2.5 V and over 500 cycles can be found in Fig. S12 in the ESI.† For $(Li_2Fe)SeO$-BM600, the data at 1C show only a small drop in capacity over more than 500 cycles when limiting the maximum voltage to 2.5 V, thereby confirming negligible fading when the formation of the $Fe_{1-x}Se_x$-phase is completely prevented. The results hence clearly show that capacity fading appearing in all previous reports on antiperovskite cathodes can be practically circumvented when the fading channel *via* $Fe_{1-x}Se_x$ is avoided.

4 Conclusions

In summary, we report for the first time a straightforward low-temperature, easy-to-scale mechanochemical synthesis method for the antiperovskite $(Li_2Fe)SeO$. Moreover, we propose a new electrochemical reaction mechanism for $(Li_2Fe)SeO$ which is generalized to all up-to-now investigated antiperovskite cathodes. Our data in particular prove the progressive partial conversion of $(Li_2Fe)SeO$ to $Fe_{1-x}Se_x$ at high voltages. While $Fe_{1-x}Se_x$ is electrochemically active its formation still reduces the overall capacity of the material and in particular opens a channel to capacity fading. Notably, completely avoiding this channel in a post-synthesis heat-treated material practically prevents capacity fading appearing in all previous reports on antiperovskite cathodes. Pristine mechanochemically synthesised $(Li_2Fe)SeO$ with more dispersed and smaller primary particles even achieves an outstanding reversible specific capacity of 200 mA h g^{-1} at the high current rate of 1C. The results and achievements presented at hand further elucidate the electrochemical reaction mechanism in antiperovskites and show a route how to increase their cycling stability. The success of this approach is already proven by the drastic performance improvements of $(Li_2Fe)SeO$ demonstrated at hand.

Author contributions

Conceptualization, L. S., M. M., N. G., R. K.; synthesis and materials characterisation, M. M., B. B., S. H., N. G.; TEM studies, I. G. G. M.; XPS studies, M. H.; BET studies, K. W., E.W.; electrochemical and magnetic studies, L. S., H. H.; writing—original draft preparation, L. S., M. M., R. K.; writing – review & editing, L. S., M. M., N. G., R. K.; visualization, L. S., M. M.; supervision, R. K. and N. G.; all authors have read and agreed to the published version of the manuscript.

Conflicts of interest

There are no conflicts to declare.

Acknowledgements

The authors thank Andrea Voss and Anne Voidel (IFW Dresden) for performing ICP-OES measurements. Financial support by

Deutsche Forschungsgemeinschaft (DFG) through projects KL 1824/20-1 and GR 5987/2-1 and by BMBF *via* the project SpinFun (13XP5088) is acknowledged. Work has also been supported within the framework of the Excellence Strategy of the Federal and State Governments of Germany *via* Heidelberg University's flagship EMS initiative. M. A. A. Mohamed thanks the IFW excellence program for financial support.

Notes and references

1 K. T. Lai, I. Antonyshyn, Y. Prots and M. Valldor, *J. Am. Chem. Soc.*, 2017, **139**, 9645–9649.
2 D. Mikhailova, L. Giebeler, S. Maletti, S. Oswald, A. Sarapulova, S. Indris, Z. Hu, J. Bednarcik and M. Valldor, *ACS Appl. Energy Mater.*, 2018, **1**, 6593–6599.
3 M. Mohamed, L. Singer, H. Hahn, D. Djendjur, A. Özkara, E. Thauer, I. G. Gonzalez-Martinez, M. Hantusch, B. Büchner, S. Hampel, R. Klingeler and N. Gräßler, *J. Power Sources*, 2023, **558**, 232547.
4 Z. Lu and F. Ciucci, *J. Mater. Chem. A*, 2018, **6**, 5185–5192.
5 M. V. Gorbunov, S. Carrocci, S. Maletti, M. Valldor, T. Doert, S. Hampel, I. G. Gonzalez Martinez, D. Mikhailova and N. Gräßler, *Inorg. Chem.*, 2020, **59**, 15626–15635.
6 M. V. Gorbunov, S. Carocci, I. G. Gonzalez Martinez, V. Baran and D. Mikhailova, *Front. Energy Res.*, 2021, **9**, 360.
7 A. Banik, T. Famprikis, M. Ghidiu, S. Ohno, M. A. Kraft and W. G. Zeier, *Chem. Sci.*, 2021, **12**, 6238–6263.
8 M. A. A. Mohamed, H. A. A. Saadallah, I. G. Gonzalez-Martinez, M. Hantusch, M. Valldor, B. Büchner, S. Hampel and N. Gräßler, *Green Chem.*, 2023, **25**, 3878–3887.
9 J. Zhang, J. Qiao, K. Sun and Z. Wang, *Particuology*, 2022, **61**, 18–29.
10 A. S. Aricò, P. Bruce, B. Scrosati, J.-M. Tarascon and W. van Schalkwijk, *Nat. Mater.*, 2005, **4**, 366–377.
11 Y. Sun, N. Liu and Y. Cui, *Nat. Energy*, 2016, **1**, 366–377.
12 R. Jain, A. S. Lakhnot, K. Bhimani, S. Sharma, V. Mahajani, R. A. Panchal, M. Kamble, F. Han, C. Wang and N. Koratkar, *Nat. Rev. Mater.*, 2022, **7**, 736–746.
13 M. A. A. Mohamed, M. V. Gorbunov, M. Valldor, S. Hampel, N. Gräßler and D. Mikhailova, *J. Mater. Chem. A*, 2021, **9**, 23095–23105.
14 P. Muhammed Shafi and A. Chandra Bose, *AIP Adv.*, 2015, **5**, 057137.
15 A. L. Patterson, *Phys. Rev.*, 1939, **56**, 978–982.
16 **http://www.gatan.com/products/tem-analysis/gatan-microscopy-suite-software**.
17 G. S. Zakharova, L. Singer, Z. A. Fattakhova, S. Wegener, E. Thauer, Q. Zhu, E. V. Shalaeva and R. Klingeler, *J. Alloys Compd.*, 2021, **863**, 158353.
18 D. Fang, F. He, J. Xie and L. Xue, *J. Wuhan Univ. Technol. Mater. Sci. Ed.*, 2020, **35**, 711–718.
19 J. F. Moulder, W. F. Stickle, W. M. Sobol and K. D. Bomben, *Handbook of X-Ray Photoelectron Spectroscopy*, 1992.
20 R. Dedryvère, M. Maccario, L. Croguennec, F. Le Cras, C. Delmas and D. Gonbeau, *Chem. Mater.*, 2008, **20**, 7164–7170.
21 T. Radu, C. Iacovita, D. Benea and R. Turcu, *Appl. Surf. Sci.*, 2017, **405**, 337–343.
22 A. P. Grosvenor, B. A. Kobe, M. C. Biesinger and N. S. McIntyre, *Surf. Interface Anal.*, 2004, **36**, 1564–1574.
23 R. Ospina, S. A. Rincón-Ortiz and J. Rodriguez-Pereira, *Surf. Sci. Spectra*, 2020, **27**, 014021.
24 J. R. Shallenberger and N. Hellgren, *Surf. Sci. Spectra*, 2020, **27**, 014020.
25 J.-C. Dupin, D. Gonbeau, P. Vinatier and A. Levasseur, *Phys. Chem. Chem. Phys.*, 2000, **2**, 1319–1324.
26 D. L. Zhang, *Prog. Mater. Sci.*, 2004, **49**, 537–560.
27 P. W. Voorhees, *J. Stat. Phys.*, 1985, **38**, 231–252.
28 M. Shi, N. Wang, B. Lei, J. Ying, C. Zhu, Z. Sun, J. Cui, F. Meng, C. Shang, L. Ma, *et al.*, *New J. Phys.*, 2018, **20**, 123007.
29 F. Nitsche, T. Goltz, H.-H. Klauss, A. Isaeva, U. Muller, W. Schnelle, P. Simon, T. Doert and M. Ruck, *Inorg. Chem.*, 2012, **51**, 7370–7376.
30 P. Terzieff and K. L. Komarek, *Monatsh. Chem.*, 1978, **109**, 1037–1047.
31 T. Hirone, S. Maeda and N. Tsuya, *J. Phys. Soc. Jpn.*, 1954, **9**, 496–499.
32 P. Terzieff and K. L. Komarek, *Monatsh. Chem.*, 1978, **109**, 651–659.
33 S. Muhammad, S. Lee, H. Kim, J. Yoon, D. Jang, J. Yoon, J.-H. Park and W.-S. Yoon, *J. Power Sources*, 2015, **285**, 156–160.
34 P. Poizot, S. Laruelle, S. Grugeon, L. Dupont and J. M. Tarascon, *Nature*, 2000, **407**, 496–499.
35 M. C. Menard, A. C. Marschilok, K. J. Takeuchi and E. S. Takeuchi, *Electrochim. Acta*, 2013, **94**, 320–326.
36 D. C. Bock, C. J. Pelliccione, W. Zhang, J. Timoshenko, K. W. Knehr, A. C. West, F. Wang, Y. Li, A. I. Frenkel, E. S. Takeuchi, K. J. Takeuchi and A. C. Marschilok, *Phys. Chem. Chem. Phys.*, 2017, **19**, 20867–20880.
37 D. Zhong, J. Chen, J. Zhang, Y. Luo, Z. Li, L. Cheng, Y. Chen, G. Wang and R. Wang, *Mater. Res. Express*, 2019, **6**, 085058.
38 Y. Lan, J. Zhou, K. Xu, Y. Lu, K. Zhang, L. Zhu and Y. Qian, *Chem. Commun.*, 2018, **54**, 5704–5707.